

Motion Measurement Errors and Autofocus in Bistatic SAR

Brian D. Rigling, *Member, IEEE*, and Randolph L. Moses *Senior Member, IEEE*

Abstract

This paper discusses the effect of motion measurement errors (MMEs) on measured bistatic synthetic aperture radar (SAR) phase history data that has been motion compensated to the scene origin. We characterize the effect of low frequency MMEs on bistatic SAR images, and based on this characterization, we derive limits on the allowable MMEs to be used as system specifications. Finally, we demonstrate that proper orientation of a bistatic SAR image during the image formation process allows application of monostatic SAR autofocus algorithms in post-processing to mitigate image defocus.

Index Terms

bistatic, SAR, motion measurement errors, ground map, autofocus.

I. INTRODUCTION

Synthetic aperture radar (SAR) imaging is an invaluable tool for aerial ground surveillance. Monostatic SAR systems, where the transmitting and receiving antennas are located on the same platform and are frequently the same antenna, have been the subject of a great deal of research and development over the past few decades. The attraction of monostatic SAR is its relative simplicity, both in system design and deployment. However, in trying to observe an area of interest at close range, a high cost monostatic platform may place itself at risk by illuminating hostile regions with its transmissions.

A growing military interest in cost effective UAV technology has sparked renewed interest in bistatic synthetic aperture radar. Bistatic SAR, as an alternative to monostatic SAR, allows a passive receiving

B.D. Rigling is with the Department of Electrical Engineering, Wright State University, 422 Russ Engineering Center, 3640 Colonel Glenn Highway, Dayton, OH 45435-0001, Email: brigling@cs.wright.edu, Phone: (937) 775-5100.

R.L. Moses is with the Department of Electrical and Computer Engineering, The Ohio State University, 205 Drees Labs, 2015 Neil Avenue, Columbus, OH 43210, E-mail:(moses@ece.osu.edu).

platform to observe at close range a scene illuminated by a remote transmitting platform. The transmitting platform may in some cases be an illuminator of opportunity, such as an overpassing satellite [1] or a local commercial transmitter. The receiving platform may be of significantly reduced cost and is far less observable due to its passive nature.

Multiple image formation processes have been developed for bistatic SAR including the backprojection algorithm (BPA) [2], matched filtering (MF) [3], direct Fourier inversion [4], and the polar format algorithm (PFA) [5]. All of these processes assume that the locations of the transmit and receive platforms are known perfectly at every point in their flight paths. However, it is well known from operational monostatic SAR systems that exact motion measurement is impossible to obtain, and a slight motion measurement error (MME) can have a drastic effect on the quality of the resulting SAR imagery.

In this paper, we analytically characterize the effects of imperfect motion measurement on bistatic SAR images. This analysis provides bounds that define the necessary precision in platform motion compensation needed to obtain usable imagery from bistatic SAR phase history data. In addition, we consider post-processing techniques for correcting MMEs, commonly known as autofocus. We show that, provided the bistatic SAR images are formed in an appropriately-chosen reference frame, monostatic autofocus techniques are applicable without modification to bistatic SAR images. In this way, the significant development in monostatic autofocus methods may be carried over to bistatic image focusing. Specifically, the bistatic SAR coordinate frame needed to apply monostatic autofocus methods is one derived via the Taylor series approximation to the bistatic differential range equation (see [5]). This approximation provides a three-dimensional generalization of the two-dimensional results in [2].

An outline of the paper is as follows. In Section II, we will describe our model for bistatic SAR phase history data collection. Section III studies how the information recorded during data collection is interpreted by image formation algorithms. Section IV describes a typical model for low frequency MMEs and analyzes their effects on the collected phase history data. In Section V, we demonstrate the effect of MMEs on bistatic SAR images. We also derive bounds on the allowable MMEs, based on limiting the degree of quadratic phase error, and we show how autofocus techniques that have been developed for monostatic SAR may be applied to bistatic SAR imagery. Finally, we summarize our conclusions in Section VI.

II. BISTATIC PHASE HISTORY DATA

Consider the bistatic SAR data collection geometry shown in Figure 1. The center of the scene to be imaged is located at the origin of coordinates, and the ground plane is the x - y plane. A scatterer

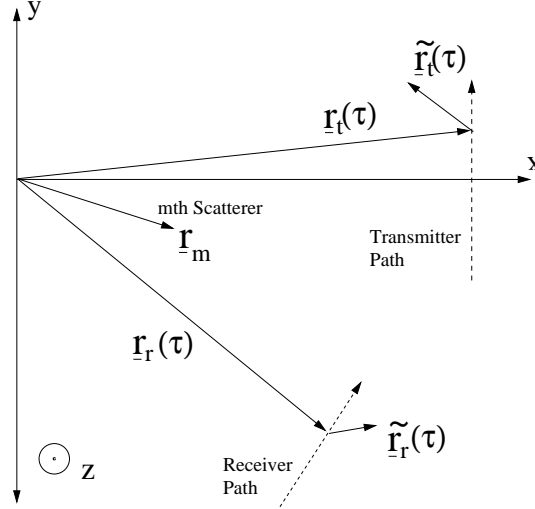


Fig. 1. Top view of a bistatic data collection geometry. The x - y plane is the ground plane.

within that scene is located at $\underline{r}_m = (x_m, y_m, z_m)$. The actual location of the transmitter at a given time τ is $\underline{r}_t(\tau) = (x_t(\tau), y_t(\tau), z_t(\tau))$. The measured transmitter location at time τ is given by $\hat{\underline{r}}_t(\tau) = \underline{r}_t(\tau) + \tilde{\underline{r}}_t(\tau)$, where $\tilde{\underline{r}}_t(\tau) = (\tilde{x}_t(\tau), \tilde{y}_t(\tau), \tilde{z}_t(\tau))$ is the location measurement error. Similarly, the actual location of the receiver at a given time τ is $\underline{r}_r(\tau) = (x_r(\tau), y_r(\tau), z_r(\tau))$, and the measured location of the receiver is $\hat{\underline{r}}_r(\tau) = \underline{r}_r(\tau) + \tilde{\underline{r}}_r(\tau)$, where $\tilde{\underline{r}}_r(\tau) = (\tilde{x}_r(\tau), \tilde{y}_r(\tau), \tilde{z}_r(\tau))$ is the receiver location measurement error.

As the transmitter moves along its flight path, the radiating antenna periodically transmits pulses of energy in the direction of the scene center. Each transmitted pulse travels from the transmitter to the scene of interest, where it is reflected by scatterers within the area of illumination. This reflected energy disperses in all directions, and some of this energy is observed by the antenna on the receiving platform. We assume that the travel time of the pulse from the transmitter to a scatterer to the receiver is sufficiently short, with respect to the pulse duration, that any platform movement within that time period may be neglected.

For clarity of exposition, we assume that transmitted pulses have uniform power over the frequency range $f \in [f_0, f_0 + B]$, where f_0 and B represent the lowest frequency and the bandwidth of the transmitted pulse, respectively. We also assume that scatterers behave as ideal point scatterers within this frequency band. These assumptions are not critical to the derivations to follow, but they do make for easier analysis. The effects of a non-uniform transmit spectrum and non-ideal scattering responses may

be incorporated into the results of Section III, and we will make a note of this at that point.

The receiver is assumed to observe delayed, band-limited impulses, with uniform power over the frequency band of interest. The delay of each pulse is the travel time from the transmitter to a scatterer to the receiver. The receiver's time of observation is gated such that an impulse reflected by a scatterer at the scene origin will have zero time delay, commonly known as motion compensation to a point. One may therefore model the received signal in the frequency domain as a complex exponential of some uniform power with a linear phase determined by the relative time delay of the transmitted pulse.

At slow time τ , the actual distance from the transmitter to the m th scatterer in the scene is $d_{tm}(\tau) = \|\underline{r}_t(\tau) - \underline{r}_m(\tau)\|$, and the actual distance from this scatterer to the receiver is $d_{rm}(\tau) = \|\underline{r}_r(\tau) - \underline{r}_m(\tau)\|$. Also at time τ , the measured distance from the transmitter to the scene origin is $d_t(\tau) = \|\underline{r}_t(\tau) + \tilde{\underline{r}}_t(\tau)\|$, and the measured distance from the receiver to the scene origin is $d_r(\tau) = \|\underline{r}_r(\tau) + \tilde{\underline{r}}_r(\tau)\|$. The time delay of the received pulse, relative to the measured travel time to and from the scene origin, may then be written as

$$t(\tau) = \frac{d_{rm}(\tau) - d_r(\tau) + d_{tm}(\tau) - d_t(\tau) + c\tilde{t}(\tau)}{c} = \frac{\Delta\hat{R}_m(\tau)}{c} \quad (1)$$

where c is the speed of light, and $\tilde{t}(\tau)$ represents the timing error between the transmitter and receiver at slow time τ . The timing error from here on will be considered to be included when we refer to MMEs. The quantity $\Delta\hat{R}_m(\tau)$ is typically known as the observed differential range of the m th scatterer [6].

Given $\Delta\hat{R}_m(\tau)$, one may define the linear phase function $\Phi_m(f_i, \tau_k)$ of the received frequency samples corresponding to a scatterer located at \underline{r}_m as

$$\Phi_m(f_i, \tau_k) = -2\pi f_i \frac{\Delta\hat{R}_m(\tau_k)}{c}, \quad i = 1 \dots N_f, k = 1 \dots N_\tau \quad (2)$$

where the f_i are the sampled frequencies, and the τ_k are the transmit-receive times. The receiver uniformly samples the frequency band $[f_0, f_0 + B]$, and the transmit-receive times $[-T/2, T/2]$ are spaced over the time it takes the transmitter to traverse its flight path. Based on the linear phase function for a single scatterer in (2), one may represent the total received signal at time τ_k and frequency f_i by the sum of the returns from all the scatterers in the scene; thus

$$S(f_i, \tau_k) = \sum_m A_m e^{j\Phi_m(f_i, \tau_k)} + w(f_i, \tau_k) \quad (3)$$

where A_m is a complex constant representing the reflection coefficient of the m th scatterer and $w(f_i, \tau_k)$ is assumed to be circular white Gaussian noise introduced by the receiver.

III. IMAGE FORMATION

To analyze the effects of MMEs on bistatic SAR imagery, we must first understand how an image formation algorithm interprets the collected phase history data to form images. The location \underline{r}_m of each scatterer in the observed scene is encoded in the phase of the observed phase histories via each differential range function $\Delta\hat{R}_m(\tau)$. One typically seeks to form SAR images by assuming that the MMEs are zero and by assuming that all of the scatterers in a scene lie on a uniform grid of pixel locations. The ML estimate of the reflectivity of a scatterer at an (x, y, z) pixel location may then be computed by using a matched filter of the form [5]

$$P(x, y, z) = \frac{1}{N_f N_\tau} \sum_{i=1}^{N_f} \sum_{k=1}^{N_\tau} S(f_i, \tau_k) e^{-j\Phi_{xyz}(f_i, \tau_k)} \quad (4)$$

where $\Phi_{xyz}(f_i, \tau_k)$ represents a phase function linearly dependent on the differential range of a scatterer located at (x, y, z) . To form a complete image, equation (4) is computed for every element of the assumed grid of (x, y, z) locations on the image plane.

As (4) is computationally inefficient, many image formation algorithms alter the method of computing the matched filter, or approximate it, in order to reduce the algorithm's complexity. A Taylor expansion of the bistatic differential range in (1) gives the first order approximation (commonly called the far-field approximation [5])

$$\Delta R \approx -\frac{xx_t + yy_t + zz_t}{\sqrt{x_t^2 + y_t^2 + z_t^2}} - \frac{xx_r + yy_r + zz_r}{\sqrt{x_r^2 + y_r^2 + z_r^2}}. \quad (5)$$

By introducing the variables ϕ_t and ϕ_r (θ_t and θ_r), denoting the azimuth (elevation) angles of the transmitter and receiver with respect to the scene center, we can write (5) in terms of these angles as

$$\begin{aligned} \Delta R(\tau_k) \approx & -x \cos(\phi_t(\tau_k)) \cos(\theta_t(\tau_k)) \\ & -y \sin(\phi_t(\tau_k)) \cos(\theta_t(\tau_k)) \\ & -z \sin(\theta_t(\tau_k)) - x \cos(\phi_r(\tau_k)) \cos(\theta_r(\tau_k)) \\ & -y \sin(\phi_r(\tau_k)) \cos(\theta_r(\tau_k)) - z \sin(\theta_r(\tau_k)) \end{aligned} \quad (6)$$

where we include the dependence on the sampled slow time τ_k . This allows use of the approximate matched filter [5]

$$\begin{aligned} P(x, y, z) \approx & \frac{1}{N_f N_\tau} \sum_{i=1}^{N_f} \sum_{k=1}^{N_\tau} S(f_i, \tau_k) \\ & \cdot \exp \left\{ -j \frac{4\pi}{c} [x f_x(f_i, \tau_k) + y f_y(f_i, \tau_k) + z f_z(f_i, \tau_k)] \right\} \end{aligned} \quad (7)$$

where

$$\begin{aligned}
f_x(f_i, \tau_k) &= \frac{f_i}{2} [\cos(\phi_t(\tau_k)) \cos(\theta_t(\tau_k)) \\
&\quad + \cos(\phi_r(\tau_k)) \cos(\theta_r(\tau_k))], \\
f_y(f_i, \tau_k) &= \frac{f_i}{2} [\sin(\phi_t(\tau_k)) \cos(\theta_t(\tau_k)) \\
&\quad + \sin(\phi_r(\tau_k)) \cos(\theta_r(\tau_k))], \\
f_z(f_i, \tau_k) &= \frac{f_i}{2} [\sin(\theta_t(\tau_k)) + \sin(\theta_r(\tau_k))].
\end{aligned} \tag{8}$$

Note that use of the far-field assumption in equation (6) introduces distortion and defocus into the final image. To limit the degree of defocus experienced, one typically limits the maximum size of an imaged scene [5]. Setting $z = 0$ (for a ground plane image) and defining the rotation of coordinates

$$\begin{aligned}
f'_x &= f_x \cos(\phi_b) + f_y \sin(\phi_b) \\
f'_y &= -f_x \sin(\phi_b) + f_y \cos(\phi_b)
\end{aligned} \tag{9}$$

and

$$\begin{aligned}
x' &= x \cos(\phi_b) + y \sin(\phi_b) \\
y' &= -x \sin(\phi_b) + y \cos(\phi_b),
\end{aligned} \tag{10}$$

where the bistatic look angle (shown in Figure 2) is

$$\begin{aligned}
\phi_b &= \arctan \left(\frac{f_y(f_i, \tau_{k_b})}{f_x(f_i, \tau_{k_b})} \right) \\
&= \arctan \left(\frac{\sin \bar{\phi}_t \cos \bar{\theta}_t + \sin \bar{\phi}_r \cos \bar{\theta}_r}{\cos \bar{\phi}_t \cos \bar{\theta}_t + \cos \bar{\phi}_r \cos \bar{\theta}_r} \right),
\end{aligned} \tag{11}$$

we obtain

$$\begin{aligned}
P(x, y, 0) &\approx \frac{1}{N_f N_\tau} \sum_{i=1}^{N_f} \sum_{k=1}^{N_\tau} S(f_i, \tau_k) \\
&\quad \cdot \exp \left\{ -j \frac{4\pi}{c} [x' f'_x(f_i, \tau_k) + y' f'_y(f_i, \tau_k)] \right\}.
\end{aligned} \tag{12}$$

We then resample the data onto the rectangular grid defined by

$$\begin{aligned}
f'_x &= f_0 + B_x \frac{k_x}{N_x}, \quad k_x = 0 \dots N_x - 1 \\
\text{and } f'_y &= \frac{-B_y}{2} + B_y \frac{k_y}{N_y}, \quad k_y = 0 \dots N_y - 1
\end{aligned} \tag{13}$$

to obtain

$$\begin{aligned}
P(x', y', 0) \approx & \frac{1}{N_x N_y} \sum_{k_x=0}^{N_x-1} \sum_{k_y=0}^{N_y-1} S(k_x, k_y) \\
& \cdot \exp \left\{ -j \frac{4\pi}{c} \left[x' \left(f_0 + B_x \frac{k_x}{N_x} \right) \right. \right. \\
& \left. \left. + y' \left(-\frac{B_y}{2} + B_y \frac{k_y}{N_y} \right) \right] \right\}
\end{aligned} \tag{14}$$

In (11), $\bar{\phi}_t$ and $\bar{\phi}_r$ ($\bar{\theta}_t$ and $\bar{\theta}_r$) represent the azimuth (elevation) angles of the transmitter and receiver at their corresponding aperture midpoints.

One may also assume that the far-field assumption holds for the observed phase history data, such that the coordinate system rotation and polar-to-rectangular interpolation converts equation (3) into the form (omitting the noise term)

$$S(k_x, k_y) \approx \sum_m A_m e^{j \frac{4\pi}{c} \left[x'_m f_0 + B_x \frac{k_x}{N_x} + y'_m \left(-\frac{B_y}{2} + B_y \frac{k_y}{N_y} \right) \right]} \tag{15}$$

where (x'_m, y'_m) is the location of the m th scatterer in the rotated coordinate system defined by (10).

Thus, applying the approximate matched filter (14) to (15) yields

$$\begin{aligned}
P(x', y', 0) \approx & \sum_m A_m e^{j \frac{2\pi}{c} \left[(x' - x'_m) \left(2f_0 + B_x - \frac{B_x}{N_x} \right) - (y' - y'_m) \frac{B_y}{N_y} \right]} \\
& \cdot \left[\frac{\sin \left(\frac{2\pi(x' - x'_m)B_x}{c} \right)}{\sin \left(\frac{2\pi(x' - x'_m)B_x}{cN_x} \right)} \right] \left[\frac{\sin \left(\frac{2\pi(y' - y'_m)B_y}{c} \right)}{\sin \left(\frac{2\pi(y' - y'_m)B_y}{cN_y} \right)} \right],
\end{aligned} \tag{16}$$

provided that there are no MMEs. We see from (16) that the scatterer location information, encoded in the observed phase histories by the differential range, determines the location of the Dirichlet kernel functions (the $[\sin(\cdot)/\sin(\cdot)]$ functions in (16)) in the image, and the width and breadth of these functions are determined by the bandwidths B_x and B_y of the phase history data.

Equation (16) is derived assuming both uniform transmit power in the frequency band $[f_0, f_0 + B]$ and flat scattering center responses. If a non-uniform transmit spectrum is used, or if scattering centers have frequency dependent responses, the resulting matched filter response will be similar to (16), but the Dirichlet kernel functions will be replaced by responses corresponding to the non-uniform spectrum and non-ideal returns. The locations of these responses in the final image, however, are still determined by the scatterer location information encoded in the observed differential range functions.

To understand the effects of MMEs in our data collection, we study the manner in which the scatterer location information is encoded in the differential range function. We first assume that the ground range $r_t = \sqrt{x_t(\tau)^2 + y_t(\tau)^2}$ and the slant range $R_t = \sqrt{x_t(\tau)^2 + y_t(\tau)^2 + z_t(\tau)^2}$ of the transmitter are

sufficiently large such that they may be treated as constants with respect to slow time τ . We make the same assumption about the ground range and slant range of the receiver, $r_r = \sqrt{x_r(\tau)^2 + y_r(\tau)^2}$ and $R_r = \sqrt{x_r(\tau)^2 + y_r(\tau)^2 + z_r(\tau)^2}$. Finally, we assume that the transmitter and receiver traverse linear flight paths at constant velocities. This allows us to write $\cos \phi(\tau) = (x_t + v_{xt}\tau)/r_t$ and $\cos \theta(\tau) = r_t/R_t$, as well as similar substitutions for the other expressions in (6). Thus, the approximated differential range in (6) may be further approximated by a linear function of slow time

$$\begin{aligned} \Delta R(\tau) &\approx -x \left(\frac{x_t + v_{xt}\tau}{r_t} \right) \left(\frac{r_t}{R_t} \right) - y \left(\frac{y_t + v_{yt}\tau}{r_t} \right) \left(\frac{r_t}{R_t} \right) - z \left(\frac{z_t + v_{zt}\tau}{R_t} \right) \\ &\quad - x \left(\frac{x_r + v_{xr}\tau}{r_r} \right) \left(\frac{r_r}{R_r} \right) - y \left(\frac{y_r + v_{yr}\tau}{r_r} \right) \left(\frac{r_r}{R_r} \right) - z \left(\frac{z_r + v_{zr}\tau}{R_r} \right) \\ &= \left[-x \left(\frac{x_t}{R_t} + \frac{x_r}{R_r} \right) - y \left(\frac{y_t}{R_t} + \frac{y_r}{R_r} \right) - z \left(\frac{z_t}{R_t} + \frac{z_r}{R_r} \right) \right] \\ &\quad \left[-x \left(\frac{v_{xt}}{R_t} + \frac{v_{xr}}{R_r} \right) - y \left(\frac{v_{yt}}{R_t} + \frac{v_{yr}}{R_r} \right) - z \left(\frac{v_{zt}}{R_t} + \frac{v_{zr}}{R_r} \right) \right] \tau \\ &\triangleq \beta_0 + \beta_1 \tau. \end{aligned} \tag{17}$$

The locations of the transmitter and receiver at their aperture midpoints are given by (x_t, y_t, z_t) and (x_r, y_r, z_r) , and the transmitter and receiver velocity vectors are (v_{xt}, v_{yt}, v_{zt}) and (v_{xr}, v_{yr}, v_{zr}) , respectively.

Equation (17) describes a transformation which relates the linear approximation of the differential range $\Delta R(\tau) = \beta_0 + \beta_1 \tau$ to the actual location of a scatterer in the scene, which is written as

$$\begin{bmatrix} \beta_0 \\ \beta_1 \end{bmatrix} = \begin{bmatrix} -\frac{x_t}{R_t} - \frac{x_r}{R_r} & -\frac{y_t}{R_t} - \frac{y_r}{R_r} & -\frac{z_t}{R_t} - \frac{z_r}{R_r} \\ -\frac{v_{xt}}{R_t} - \frac{v_{xr}}{R_r} & -\frac{v_{yt}}{R_t} - \frac{v_{yr}}{R_r} & -\frac{v_{zt}}{R_t} - \frac{v_{zr}}{R_r} \end{bmatrix} \begin{bmatrix} x \\ y \\ z \end{bmatrix}. \tag{18}$$

We will focus on scatterers located on the ground plane ($z = 0$), giving

$$\begin{bmatrix} \beta_0 \\ \beta_1 \end{bmatrix} = \begin{bmatrix} -\frac{x_t}{R_t} - \frac{x_r}{R_r} & -\frac{y_t}{R_t} - \frac{y_r}{R_r} \\ -\frac{v_{xt}}{R_t} - \frac{v_{xr}}{R_r} & -\frac{v_{yt}}{R_t} - \frac{v_{yr}}{R_r} \end{bmatrix} \begin{bmatrix} x \\ y \end{bmatrix} \triangleq Q \begin{bmatrix} x \\ y \end{bmatrix}. \tag{19}$$

Therefore, given a measured differential range function for a single scatterer on the ground, one may linearly approximate $\Delta R(\tau)$ and then use

$$\begin{bmatrix} x \\ y \end{bmatrix} = Q^{-1} \begin{bmatrix} \beta_0 \\ \beta_1 \end{bmatrix} \tag{20}$$

to estimate the (x, y) location of that scatterer's response, as defined by (16), in a ground plane image.

From (16) and (19), we make two important observations. First, from (16) we see that the accuracy with which we may extract location information from the recorded phase histories is determined by the

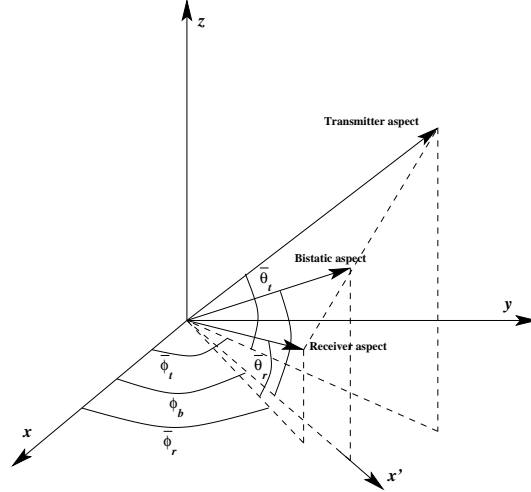


Fig. 2. The bistatic aspect bisects the solid angle between the transmitter and receiver aspects in three-dimensional space.

bandwidths of the data in range (B_x) and crossrange (B_y). Second, provided there are no MMEs, the (x, y) location of a scatterer in the ground plane is encoded in the differential range ($\beta_0 = \Delta R(\tau)$) and its time derivative ($\beta_1 = \Delta R'(\tau)$) at every point in the data collection through the linear mapping Q .

IV. CHARACTERIZING MOTION MEASUREMENT ERRORS

The above derivations assume that there are no MMEs. To implement an actual bistatic SAR system, MMEs must be considered. Errors in measuring the motion of an airborne surveillance platform have frequently been characterized [6]–[9] by expressions in the form

$$\tilde{r}(\tau) = \underline{\tilde{g}}(\tau) + \tilde{h}(\tau) \quad (21)$$

where $\underline{\tilde{g}}(\tau)$ represents low frequency errors, and $\tilde{h}(\tau)$ represents high frequency errors. The low frequency component of the errors is often modeled as a polynomial, whereas the high frequency errors are more difficult to model and are most often described by their spectral characteristics or RMS values. The high frequency errors are usually much smaller in magnitude than the low frequency errors, and typically consist of noise-like elements, and sinusoidal components with periods much shorter than the aperture duration. Errors not due to motion measurement, such as propagation phenomena and atmospheric turbulence, also contribute to the high frequency errors. We will focus on the dominant low frequency elements of the unmeasured platform motion, and we will model them with a quadratic polynomial in

the form

$$\underline{\tilde{g}}(\tau) = \begin{bmatrix} \tilde{x}(\tau) \\ \tilde{y}(\tau) \\ \tilde{z}(\tau) \end{bmatrix} = \begin{bmatrix} \tilde{p}_x \\ \tilde{p}_y \\ \tilde{p}_z \end{bmatrix} + \begin{bmatrix} \tilde{v}_x \\ \tilde{v}_y \\ \tilde{v}_z \end{bmatrix} \tau + \begin{bmatrix} \tilde{a}_x \\ \tilde{a}_y \\ \tilde{a}_z \end{bmatrix} \frac{\tau^2}{2} \quad (22)$$

where $[\tilde{p}_x \ \tilde{p}_y \ \tilde{p}_z]^T$ represents the error in measuring the platform's location at the aperture midpoint, and $[\tilde{v}_x \ \tilde{v}_y \ \tilde{v}_z]^T$ and $[\tilde{a}_x \ \tilde{a}_y \ \tilde{a}_z]^T$ represent the errors in measuring the platform's velocity and acceleration.

By applying to $\Delta\tilde{R}(\tau)$ the same approximations used to arrive at (17), we can approximate the error introduced into the observed differential range as

$$\begin{aligned} \Delta\tilde{R}(\tau) \approx & -\tilde{x}_t(\tau) \frac{x_t + v_{xt}\tau}{R_t} - \tilde{x}_r(\tau) \frac{x_r + v_{xr}\tau}{R_r} \\ & -\tilde{y}_t(\tau) \frac{y_t + v_{yt}\tau}{R_t} - \tilde{y}_r(\tau) \frac{y_r + v_{yr}\tau}{R_r} \\ & -\tilde{z}_t(\tau) \frac{z_t + v_{zt}\tau}{R_t} - \tilde{z}_r(\tau) \frac{z_r + v_{zr}\tau}{R_r} + c\tilde{t}(\tau). \end{aligned} \quad (23)$$

Using (23), we may characterize the effect of motion measurement errors on the observed differential range, by substituting in the quadratic polynomial expressions for the MMEs $\{\tilde{x}_t(\tau), \tilde{x}_r(\tau), \tilde{y}_t(\tau), \tilde{y}_r(\tau), \tilde{z}_t(\tau), \tilde{z}_r(\tau)\}$ in (22). In addition, we will assume that the time synchronization error between the transmit and receive platforms is of the form $\tilde{t}(\tau) = \tilde{t}_0 + \tilde{t}_1\tau + \tilde{t}_2\tau^2 + \tilde{t}_3\tau^3$. The result is a cubic polynomial expression for (23), $\Delta\tilde{R}(\tau) \approx \tilde{\beta}_0 + \tilde{\beta}_1\tau + \tilde{\beta}_2\tau^2 + \tilde{\beta}_3\tau^3$. Table I shows the errors in the observed differential range induced by transmitter MMEs and time synchronization errors. The errors induced by receiver MMEs are identical. In Section V, the results in Table I will allow us to study the effect of MMEs on bistatic SAR images.

V. EFFECT OF MOTION MEASUREMENT ERRORS ON BISTATIC SAR IMAGES

The results of the previous section allow us to approximate the observed differential range as

$$\begin{aligned} \Delta\hat{R}(\tau) & \approx \hat{\beta}_0 + \hat{\beta}_1\tau + \hat{\beta}_2\tau^2 + \hat{\beta}_3\tau^3 \\ & \triangleq (\beta_0 + \tilde{\beta}_0) + (\beta_1 + \tilde{\beta}_1)\tau + \tilde{\beta}_2\tau^2 + \tilde{\beta}_3\tau^3. \end{aligned} \quad (24)$$

We may determine the impact of differential range errors on bistatic SAR images by using the results of Section III to study (24). The image domain effects of constant and linear differential range errors are

TABLE I
EXAMPLES OF TRANSMITTER MME INDUCED DIFFERENTIAL RANGE ERRORS.

MME	$\Delta\tilde{R}(\tau)$			
	Constant ($\tilde{\beta}_0$)	Linear ($\tilde{\beta}_1$)	Quadratic ($\tilde{\beta}_2$)	Cubic ($\tilde{\beta}_3$)
$\tilde{t}(\tau)$	$c\tilde{t}_0$	$c\tilde{t}_1$	$c\tilde{t}_2$	$c\tilde{t}_3$
$\tilde{x}_t(\tau) = \tilde{p}_{xt}$	$-\frac{\tilde{p}_{xt}x_t}{R_t}$	$-\frac{\tilde{p}_{xt}v_{xt}}{R_t}$	-	-
$\tilde{x}_t(\tau) = \tilde{v}_{xt}\tau$	-	$-\frac{\tilde{v}_{xt}x_t}{R_t}$	$-\frac{\tilde{v}_{xt}v_{xt}}{R_t}$	-
$\tilde{x}_t(\tau) = \frac{1}{2}\tilde{a}_{xt}\tau^2$	-	-	$-\frac{\tilde{a}_{xt}x_t}{2R_t}$	$-\frac{\tilde{a}_{xt}v_{xt}}{2R_t}$
$\tilde{y}_t(\tau) = \tilde{p}_{yt}$	$-\frac{\tilde{p}_{yt}y_t}{R_t}$	$-\frac{\tilde{p}_{yt}v_{yt}}{R_t}$	-	-
$\tilde{y}_t(\tau) = \tilde{v}_{yt}\tau$	-	$-\frac{\tilde{v}_{yt}y_t}{R_t}$	$-\frac{\tilde{v}_{yt}v_{yt}}{R_t}$	-
$\tilde{y}_t(\tau) = \frac{1}{2}\tilde{a}_{yt}\tau^2$	-	-	$-\frac{\tilde{a}_{yt}y_t}{2R_t}$	$-\frac{\tilde{a}_{yt}v_{yt}}{2R_t}$
$\tilde{z}_t(\tau) = \tilde{p}_{zt}$	$-\frac{\tilde{p}_{zt}z_t}{R_t}$	$-\frac{\tilde{p}_{zt}v_{zt}}{R_t}$	-	-
$\tilde{z}_t(\tau) = \tilde{v}_{zt}\tau$	-	$-\frac{\tilde{v}_{zt}z_t}{R_t}$	$-\frac{\tilde{v}_{zt}v_{zt}}{R_t}$	-
$\tilde{z}_t(\tau) = \frac{1}{2}\tilde{a}_{zt}\tau^2$	-	-	$-\frac{\tilde{a}_{zt}z_t}{2R_t}$	$-\frac{\tilde{a}_{zt}v_{zt}}{2R_t}$

straightforward to analyze. By inserting the observed $(\hat{\beta}_0, \hat{\beta}_1)$ into (20) to get

$$\begin{aligned}
\begin{bmatrix} \hat{x} \\ \hat{y} \end{bmatrix} &= Q^{-1} \begin{bmatrix} \hat{\beta}_0 \\ \hat{\beta}_1 \end{bmatrix} = Q^{-1} \begin{bmatrix} \beta_0 + \tilde{\beta}_0 \\ \beta_1 + \tilde{\beta}_1 \end{bmatrix} \\
&= \begin{bmatrix} x \\ y \end{bmatrix} + Q^{-1} \begin{bmatrix} \tilde{\beta}_0 \\ \tilde{\beta}_1 \end{bmatrix} \triangleq \begin{bmatrix} x \\ y \end{bmatrix} + \begin{bmatrix} \tilde{x} \\ \tilde{y} \end{bmatrix}, \tag{25}
\end{aligned}$$

we see that the dominant effect of constant and linear differential range errors is a spatially invariant shift in the imaged location of any scatterer in the scene, such that a scatterer located at (x, y) in the scene will yield a sinc response (16) in the image at $(\hat{x}, \hat{y}) = (x, y) + (\tilde{x}, \tilde{y})$.

For terms in the observed differential range function that are quadratic or cubic in τ , the effect of the errors are analyzed indirectly. To perform this analysis, we will make use of the results from Section III, which indicated that image formation processes extract the scatterer location information that is encoded in $\Delta\hat{R}(\tau)$ and $\Delta\hat{R}'(\tau)$, at every point in the aperture, and places a Dirichlet kernel function, with a spread determined by B_x and B_y , at that location. We therefore approximate quadratic or cubic terms in

$\Delta\tilde{R}(\tau)$ with a piece-wise linear function of the form

$$\Delta\tilde{R}(\tau) \approx \tilde{\beta}_{0,i} + \tilde{\beta}_{1,i}\tau, \quad \tau_i - \frac{\delta_\tau}{2} \leq \tau < \tau_i + \frac{\delta_\tau}{2} \quad (26)$$

$$\tilde{\beta}_{0,i} = \Delta\tilde{R}(\tau_i) \quad (27)$$

$$\tilde{\beta}_{1,i} = \frac{\partial\Delta\tilde{R}(\tau_i)}{\partial\tau} \quad (28)$$

where δ_τ is the width of each piece-wise linear interval, and the τ_i are the centers of those intervals. This piece-wise linear decomposition serves as the basis for the map drift autofocus algorithm [10] for monostatic SAR. Each matrix Q_i , and each $\beta_{0,i}$ and $\beta_{1,i}$, is computed based on the locations of the transmitter and receiver at the time interval midpoints τ_i . For a linear flight path, the $\beta_{1,i}$ should all equal the original β_1 . We can now interpret the observed differential range function by computing the location

$$\begin{aligned} \begin{bmatrix} \hat{x}_i \\ \hat{y}_i \end{bmatrix} &= Q_i^{-1} \begin{bmatrix} \hat{\beta}_{0,i} \\ \hat{\beta}_{1,i} \end{bmatrix} = Q_i^{-1} \begin{bmatrix} \beta_{0,i} + \tilde{\beta}_{0,i} \\ \beta_{1,i} + \tilde{\beta}_{1,i} \end{bmatrix} \\ &= \begin{bmatrix} x_i \\ y_i \end{bmatrix} + Q_i^{-1} \begin{bmatrix} \tilde{\beta}_{0,i} \\ \tilde{\beta}_{1,i} \end{bmatrix} \end{aligned} \quad (29)$$

that each linear sub-interval indicates. The resulting $\{(\hat{x}_i, \hat{y}_i)\}$ are the approximate locations of the broadened Dirichlet responses resulting from each sub-aperture, which will add by superposition in the final image. Without MMEs, these responses add coherently to form a sharpened response, but in the presence of errors in $\Delta\hat{R}(\tau)$ that are of quadratic or higher order, a smeared response will appear. We may also note that the primary effect of the MMEs, modeled by $Q_i^{-1}[\tilde{\beta}_{0,i} \ \tilde{\beta}_{1,i}]^T$, is independent of the location (x_i, y_i) of the observed scatterer. These defocusing effects are therefore considered spatially invariant.

To illustrate the above approach, we consider a bistatic scenario where, at their aperture midpoints, the transmitter range is 31 kilometers, the receiver range is 8.5 kilometers, and the transmitter and receiver have an angular separation of 45 degrees in azimuth. Both platforms view the scene at broadside, and the total data collection time is approximately $T = 6$ seconds. The measured motion of the transmitter includes an uncompensated acceleration of 0.005 m/s^2 in the x direction, which gives an observed differential range function with the quadratic component shown in Figure 3. We compute $\{(\hat{\beta}_{0,i}, \hat{\beta}_{1,i}) | i = 1, 2, 3\}$ from (27)–(28) to approximate the quadratic component of the differential range error with three line segments, as shown in Figure 3. We then compute the image domain locations $\{(\hat{x}_i, \hat{y}_i) | i = 1, 2, 3\}$ from (29). These three points are plotted in Figure 4. The image shown in Figure 5 was formed from the phase histories resulting from inserting the observed $\Delta\hat{R}(\tau)$ into Equation (3). We observe that a line segment

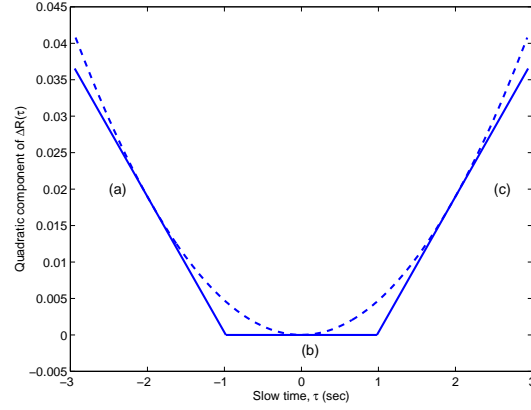


Fig. 3. Quadratic component of the differential range function induced by an uncompensated 0.005 m/s^2 acceleration of the transmitter in the x direction.

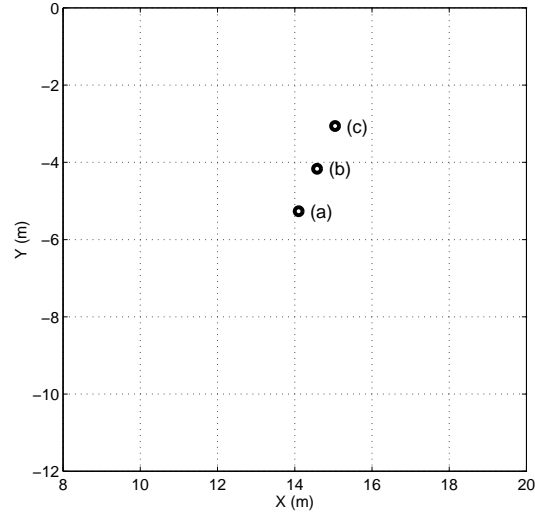


Fig. 4. Approximate image domain locations corresponding to the three line segments used to approximate $\Delta R(\tau)$ in Figure 3.

connecting the points $\{(\hat{x}_i, \hat{y}_i) | i = 1, 2, 3\}$ accurately predicts the direction of main lobe broadening that appears in the final image.

To understand why the defocus seen in Figure 5 is predominantly in a single direction, we may analyze

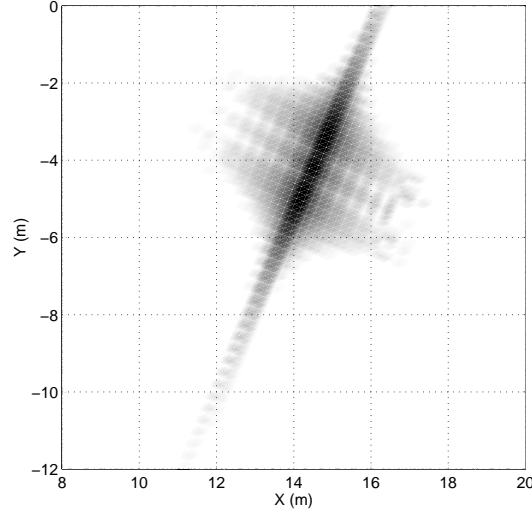


Fig. 5. Ground plane image (formed in the global (x, y) coordinate system using equation (4)) of the smeared response caused by an uncompensated 0.005 m/s^2 acceleration of the transmit platform in the x direction. Without this MME, a focused response would appear instead.

the inverses of the Q_i matrices. From (6), (19) and (20), we may write

$$\begin{aligned} Q_i^{-1} &= \frac{1}{|Q_i|} \begin{bmatrix} -\frac{v_{yt}}{R_t} - \frac{v_{yr}}{R_r} & \frac{y_t(\tau_i)}{R_t} + \frac{y_r(\tau_i)}{R_r} \\ \frac{v_{xt}}{R_t} + \frac{v_{xr}}{R_r} & -\frac{x_t(\tau_i)}{R_t} - \frac{x_r(\tau_i)}{R_r} \end{bmatrix} \\ &= \frac{1}{|Q_i|} \begin{bmatrix} -\frac{v_{yt}}{R_t} - \frac{v_{yr}}{R_r} & \sin \phi_t(\tau_i) \cos \theta_t(\tau_i) + \sin \phi_r(\tau_i) \cos \theta_r(\tau_i) \\ \frac{v_{xt}}{R_t} + \frac{v_{xr}}{R_r} & -\cos \phi_t(\tau_i) \cos \theta_t(\tau_i) - \cos \phi_r(\tau_i) \cos \theta_r(\tau_i) \end{bmatrix} \end{aligned} \quad (30)$$

where $\phi_t(\tau_i)$ and $\phi_r(\tau_i)$ ($\theta_t(\tau_i)$ and $\theta_r(\tau_i)$) are the azimuth (elevation) angles of the transmitter and receiver at the sub-aperture midpoints. Since R_t and R_r are typically on the order of several kilometers and $\sqrt{v_{xt}^2 + v_{yt}^2}$ and $\sqrt{v_{xr}^2 + v_{yr}^2}$ are typically a few hundred meters per second at most, the norm of the first column of Q_i^{-1} will be much smaller than the norm of the second column. Furthermore, the vector $[\sin \phi_t(\tau_i) \cos \theta_t(\tau_i) + \sin \phi_r(\tau_i) \cos \theta_r(\tau_i) \quad -\cos \phi_t(\tau_i) \cos \theta_t(\tau_i) - \cos \phi_r(\tau_i) \cos \theta_r(\tau_i)]^T$ does not vary significantly across the aperture.

Thus, we see that terms of $\Delta \tilde{R}(\tau)$ that are of quadratic or higher order will cause a smearing in the image that is primarily in the direction of

$$\underline{v}_{\text{defocus}} = \begin{bmatrix} \sin \bar{\phi}_t \cos \bar{\theta}_t + \sin \bar{\phi}_r \cos \bar{\theta}_r \\ -\cos \bar{\phi}_t \cos \bar{\theta}_t - \cos \bar{\phi}_r \cos \bar{\theta}_r \end{bmatrix}. \quad (31)$$

It is significant to note that $\underline{v}_{\text{defocus}}$ is orthogonal to the bistatic SAR range direction $[\cos \bar{\phi}_t \cos \bar{\theta}_t +$

$$\cos \bar{\phi}_r \cos \bar{\theta}_r \\ \sin \bar{\phi}_t \cos \bar{\theta}_t + \sin \bar{\phi}_r \cos \bar{\theta}_r]^T \text{ indicated by (11).}$$

We next derive system specifications that will limit the degree of defocus in the final image. In monostatic SAR systems, one typically chooses to limit the magnitude of quadratic phase error (QPE) contributed by any one motion measurement error to be less than $\pi/4$ radians [6]. As we are considering a bistatic system, which is dependent on two antenna platforms, we choose to limit our QPEs to be less than $\pi/8$ radians for each platform. To determine the QPE caused by each form of motion measurement error, we insert $\Delta \tilde{R}(\tau)$ into the phase function given in (2) to obtain an expression for the phase error $\tilde{\Phi}$. We then limit the quadratic component of $\tilde{\Phi}$ to be less than $\pi/8$ radians to arrive at the transmitter specifications given in Table II. Recall that the length of the total data collection time interval is represented by T . The motion measurement specifications for the receiving platform are obtained from Table II by replacing “t” subscripts with “r” subscripts. We note that the elements in Table II generalize the monostatic SAR case, and agree with the expressions in [6, Table 5.7 and 5.12] for the size of quadratic phase errors from major sources and for the allowable motion levels, if one sets the broadening factor K_a to one and takes into account a rotation of coordinate systems. Note that in general the allowable motion requirements need not be split equally between the transmitter and receiver, as it is the aggregate position uncertainty that matters.

Higher order phase errors are less dominant in SAR images, are more difficult to analyze, and have consequently been given less treatment in the SAR literature. Typically for monostatic SAR, the allowable levels of high frequency vibrations are determined based on image quality metrics such as the peak side lobe ratio (PSLR) and the integrated side lobe ratio (ISLR) [6]. In [6, Table 5.12], the allowable sinusoidal motion is specified through a PSLR-dependent limitation on the sinusoid amplitude $A_s \leq \lambda/(2\pi)\sqrt{PSLR}$, and the allowable wide band vibration level is specified with an ISLR-dependent limitation on the RMS vibration value $\sigma_v \leq \lambda/(2\pi)\sqrt{ISLR}$. We may easily extend these limits to bistatic SAR by simply splitting the RMS values of both between the transmitter and receiver. Dividing the requirements equally gives a sinusoidal requirement $A_{t/r} \leq \lambda/(2\pi)\sqrt{PSLR/2}$ and an RMS vibration requirement $\sigma_{t/r} \leq \lambda/(2\pi)\sqrt{ISLR/2}$. The allowable motion may be divided unequally provided that the total RMS value does not exceed that which is specified by [6].

VI. BISTATIC SAR AUTOFOCUS

We next turn to the problem of image post-processing techniques to reduce the defocusing effects of MMEs. The analysis of the previous section provides such a mechanism. Two points from that analysis

TABLE II

QUADRATIC PHASE ERRORS (QPE) CORRESPONDING TO TRANSMIT PLATFORM LOCATION, VELOCITY, AND ACCELERATION MME, AND MAXIMUM ALLOWABLE MME TO PREVENT IMAGE DEFOCUS.

MME	QPE	Allowable MME
$\tilde{x}_t(\tau) = \tilde{v}_{xt}\tau$	$\frac{\pi \tilde{v}_{xt} v_{xt} T^2}{2\lambda R_t}$	$\tilde{v}_{xt} < \frac{\lambda R_t}{4v_{xt} T^2}$
$\tilde{y}_t(\tau) = \tilde{v}_{yt}\tau$	$\frac{\pi \tilde{v}_{yt} v_{yt} T^2}{2\lambda R_t}$	$\tilde{v}_{yt} < \frac{\lambda R_t}{4v_{yt} T^2}$
$\tilde{z}_t(\tau) = \tilde{v}_{zt}\tau$	$\frac{\pi \tilde{v}_{zt} v_{zt} T^2}{2\lambda R_t}$	$\tilde{v}_{zt} < \frac{\lambda R_t}{4v_{zt} T^2}$
$\tilde{x}_t(\tau) = \frac{1}{2} \tilde{a}_{xt} \tau^2$	$\frac{\pi \tilde{a}_{xt} x_t T^2}{4\lambda R_t}$	$\tilde{a}_{xt} < \frac{\lambda}{2T^2 \cos(\bar{\phi}_t) \cos(\bar{\theta}_t)}$
$\tilde{y}_t(\tau) = \frac{1}{2} \tilde{a}_{yt} \tau^2$	$\frac{\pi \tilde{a}_{yt} y_t T^2}{4\lambda R_t}$	$\tilde{a}_{yt} < \frac{\lambda}{2T^2 \sin(\bar{\phi}_t) \cos(\bar{\theta}_t)}$
$\tilde{z}_t(\tau) = \frac{1}{2} \tilde{a}_{zt} \tau^2$	$\frac{\pi \tilde{a}_{zt} z_t T^2}{4\lambda R_t}$	$\tilde{a}_{zt} < \frac{\lambda}{2T^2 \sin(\bar{\theta}_t)}$

Note: Expressions for receiving platform errors are obtained by replacing $(\cdot)_t$ with $(\cdot)_r$.

are significant. First, the smearing due to MMEs is concentrated primarily in one direction, defined by (31). The significance of that point is that in the bistatic case, as in the monostatic case, it is typically sufficient to apply autofocus algorithms in only one of the two image dimensions. Second, the defocus is always in the direction orthogonal to the bistatic angle ϕ_b in (10). Thus, if bistatic images are formed using this direction as the “downrange”, defocus is primarily in crossrange (just as in the monostatic case), and monostatic autofocus algorithms can be applied without modification.

The above two observations lead to two ways in which bistatic autofocus can be implemented with existing monostatic autofocus methods. For generally-chosen image coordinate systems (such as an absolute frame of reference (x, y) as in Figure 1), bistatic autofocus methods can consist of an image rotation, followed by application of monostatic autofocus, followed by a rotation back. However, for a particular choice of reference frame, the rotation operations can be eliminated. Since the MME defocus is concentrated in the direction orthogonal to ϕ_b in (10), we can choose to form bistatic images in the (x', y') coordinate system using (14) (see also [5]), where the bistatic downrange direction x' is aligned with ϕ_b (see (10) and Figure 2). In this case, the defocus is always in the “bistatic crossrange” direction, just as in the monostatic case; thus, any of several available monostatic autofocus algorithms can be applied directly to bistatic imagery. In either case above, we can take advantage of the significant development of monostatic autofocus algorithms (e.g., [6], [7], [10]–[13]) to enhance bistatic imagery that has been

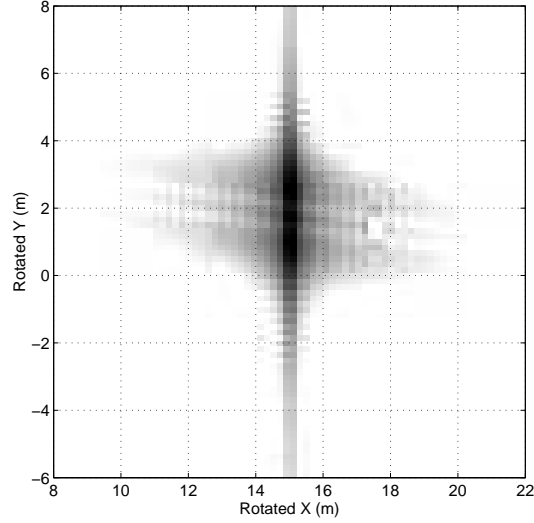


Fig. 6. Image with MME effects that has been formed in the rotated (x', y') coordinate system, using equation (14), such that the majority of the defocus is in the crossrange (y') direction. This is equivalent to the image of Figure 5 rotated by ϕ_b .

degraded by MMEs.

We illustrate the above process with an example. Figure 5 shows the defocused bistatic image in the absolute (x, y) coordinate system defined in Figure 1, formed using equation (4). Similarly, Figure 6 shows the defocused bistatic SAR images in the rotated (x', y') coordinate system. This image is formed using equation (14); alternately, one could perform a rotation on the image in Figure 5. In Figure 6, the defocus is primarily in the crossrange (y') direction. Any of several standard monostatic autofocus algorithms can now be applied to the image in Figure 6. As an example, we have applied a popular monostatic algorithm, namely the phase gradient algorithm [11], [12] to obtain the focused response shown in Figure 7. As in monostatic SAR, a reliable autofocus algorithm with the ability to correct πN_{pull} radians of QPE will increase the allowable maximum MMEs in the third column of Table II by a factor of $4N_{pull}$.

VII. CONCLUSIONS

In this paper, we introduced a model for bistatic SAR data collection. We used this model to study bistatic SAR image formation processes and the principal effects of motion measurement errors on the resulting images. We found that low frequency motion measurement errors, resulting in quadratic or higher order phase errors, primarily cause spatially invariant defocus in a direction orthogonal to the bistatic look angle. As a result, we demonstrated that autofocus algorithms for monostatic SAR may be applied to

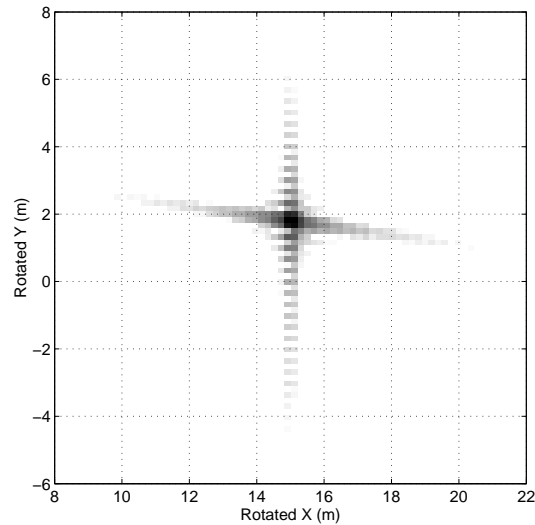


Fig. 7. Image with MME effects after application of phase gradient algorithm autofocus. Rotation by $-\phi_b$ into the global (x, y) reference frame would complete the image formation process.

bistatic SAR images, after an appropriate image rotation. We also derived expressions for the maximum allowable errors on transmit and receive platform location, velocity, and acceleration measurements to maintain focused bistatic images. These expressions generalize corresponding measurement error equations for the monostatic case.

REFERENCES

- [1] C. Mikhail, K. Kurt and N. David, "Bistatic synthetic aperture radar with non-cooperative LEOS based transmitter," *IEEE 2000 International Geoscience and Remote Sensing Symposium Proceedings*, vol. 2, pp. 861–862, 2000.
- [2] O. Arikan and D.C. Munson, "A Tomographic Formulation of Bistatic Synthetic Aperture Radar," *Proc. ComCon '88*, p. 418, October 1988.
- [3] A.D.M. Garvin and M.R. Inggs, "Use of Synthetic Aperture and Stepped-Frequency Continuous Wave Processing to Obtain Radar Images," *South African Symposium on Communications and Signal Processing 1991*, pp. 32–35, 1991.
- [4] M. Soumekh, "Bistatic Synthetic Aperture Radar Inversion with Application in Dynamic Object Imaging," *IEEE Transactions on Signal Processing*, vol. 39, pp. 2044–2055, September 1991.
- [5] B.D. Rigling and R.L. Moses, "Polar Format Algorithm for Bistatic SAR," *Submitted to IEEE Transactions on Aerospace and Electronic Systems*, June 2002.
- [6] W.G. Carrara, R.S. Goodman and R.M. Majewski, *Spotlight Synthetic Aperture Radar: Signal Processing Algorithms*. Norwood, MA: Artech House, 1995.
- [7] C.V. Jakowatz, D.E. Wahl and P.H. Eichel, *Spotlight-Mode Synthetic Aperture Radar: A Signal Processing Approach*. Boston, MA: Kluwer Academic Publishers, 1996.

- [8] D. Blacknell *et al.*, “Geometric Accuracy in Airborne SAR Images,” *IEEE Transactions on Aerospace and Electronic Systems*, vol. 25, pp. 241–257, March 1989.
- [9] T.A. Kennedy, “Strapdown Inertial Measurement Units for Motion Compensation for Synthetic Aperture Radars,” *IEEE AES Magazine*, October 1988.
- [10] C.E. Mancill and J.M. Swiger, “A Map Drift Autofocus Technique for Correcting Higher Order SAR Phase Errors (U),” *27th Annual Tri-Service Radar Symposium Record*, pp. 391–400, June 1981.
- [11] P.H. Eichel and C.V. Jakowatz, Jr., “Phase-Gradient Algorithm as an Optimal Estimator of the Phase Derivative,” *Optics Letters*, vol. 14, pp. 1101–1109, October 1989.
- [12] D.E. Wahl *et al.*, “Phase Gradient Autofocus—A Robust tool for High Resolution SAR Phase Correction,” *IEEE Transactions on Aerospace and Electronic Systems*, vol. 30, pp. 827–834, July 1994.
- [13] W.D. Brown and D.C. Ghiglia, “Some Methods for Reducing Propagation-Induced Phase Errors in Coherent Imaging Systems. I. Formalism,” *Journal of the Optical Society of America A*, vol. 5, pp. 924–942, June 1988.